

## Chapter 3

# Data Reduction of Image Plate Data Using FIT2D

A large part of the X-ray powder diffraction data described in this thesis were collected with an imaging plate detector. These data were processed and converted into tables of scattered intensities *versus* scattering angle  $2\Theta$  employing the computer program FIT2D (Hammersley et al., 1998). This chapter describes the parasitic diffraction phenomena and the corrections that need to be applied to the image plate data along with the procedures of how the corrections were made with FIT2D.

### 3.1 The Problem

As described in Chapter 2, diffracted intensity in a powder diffraction experiment is observed on a set of Debye-Scherrer cones. Detection of the diffracted radiation can geometrically be seen as the intersection of the set of Debye-Scherrer cones with a surface that represents all possible locations of the detector. The intersection of the Debye-Scherrer cones with a plane, which can be regarded as the detection plane of an imaging plate detector that is aligned perpendicular to the axes of the Debye-Scherrer cones, results in a set of concentric rings (denoted Debye-Scherrer Rings or powder rings) on the detection plane (Fig. 3.1). The radii of the rings contain information about the diffraction angles and in the ideal case, the intensity on a ring is homogeneous and does not depend on the azimuth. Real powder rings however, are more or less spotty or discontinuous. This effect is demonstrated for  $\text{In}_x\text{Nb}_3\text{Te}_4$  (Chapter 5). In the case of a large irradiated volume (many particles) the powder rings appear homogeneous (Fig. 3.1), while for a small sample volume the powder rings are spotty (Fig. 3.2). The latter type of experiment is typical for the small volumes in diamond anvil cells, and it shows the fundamental problems with data quality, for data that are collected in high-pressure experiments. For homogeneous Debye-Scherrer rings the intensity

as a function of the ring radius can be measured by scanning a narrow stripe of the image in radial direction (from the center outward). The resulting table of intensity *versus* ring radius ( $r$ ) is equivalent to data collected in a conventional powder diffraction experiment with a point detector mounted on the  $2\Theta$ -arm of a goniometer. If the same procedure is applied to inhomogeneous or discontinuous Debye-Scherrer rings, intensities would be obtained, which are dependent on the direction of the radial scan. To get reliable values of the intensities, one has to do averaging over several radial scans taken along different azimuthal directions or over larger continuous segments of the Debye-Scherrer rings. The most accurate intensities are obtained, when complete or almost complete rings are used. Since the positions of all powder rings on an image are not known, the complete image plate recording has to be integrated along the azimuthal coordinate ( $\phi$ ). In the ideal case the integration is made along circles with radius  $r$  around the center of the Debye-Scherrer rings for  $r$  ranging from zero up to the border of the detector. The position of the center of the Debye-Scherrer rings on the image (denoted as beam center) is represented by two parameters ( $x_0$  and  $y_0$  coordinates). The ideal case (integration along circles) only applies, if the detector is perfectly aligned perpendicular to the incident beam. Normally this is not the case and the Debye-Scherrer rings on the image are slightly distorted and thus have an elliptical shape. The integration has to be made along curves that represent the shapes of the Debye-Scherrer rings. The sizes of the ellipses are given by one independent variable: an effective radius  $r$  that replaces the radius of the circles. Two parameters are required to describe the shape and the orientation of the integration ellipses. One of them is the angle between the principal axes of the ellipses and the coordinate axes of the image in the detector plane (tilt plane rotation angle). The other parameter is the angle between the normal of the detection plane and the direction of the incident beam (tilt angle). If wrong values for these two angles or the beam center coordinates are used for the integration, the Bragg peaks in the integrated powder pattern would suffer from peak broadening, irregular peak shapes, and wrong intensities. All four geometric parameters have to be known prior to the integration. They can be determined using the shapes of the Debye-Scherrer rings, *i.e.* information present on the diffraction images. Therefore the integration of the diffraction images is possible without any additional information, but then it would provide data of intensity *versus* effective radius  $r$ . This data has to be converted to data of intensity *versus* diffraction angle  $2\Theta$  or d-spacing, in order to be used in Rietveld refinement computer programs. To do the conversion, two additional parameters are required: the wavelength of the radiation and the distance between the sample and the detector. To determine these two parameters, additional information, not present in the image, is required - the lattice parameters of the measured compound. Errors at the stage of conversion introduce a systematic shift to the positions of the Bragg peaks in the integrated pattern and this systematic shift also affects the

lattice parameters. The intensities of the Bragg peaks are unaffected. In section 3.4 it will be described, how all six geometric parameters can be obtained with FIT2D.

Conventional Rietveld refinement programs are designed to work with data obtained from point detectors. Similar information is obtained for integrated image plate recordings, if the intensities are scaled by the circumference of the integration ellipses. Rather frequently, however, powder rings on an image plate recording are not complete, *e.g.* larger segments of rings can be outside the detection area if the detector was misaligned (Fig. 3.3). A shift of the detector relative to the beam can even be deliberate, because in this way the angular range and so the total number of Debye-Scherrer rings on an image can be increased. Using a shorter sample-to-detector distance would have the same effect, but there is a minimum distance, which is imposed by the spatial resolution of the image plate detector. Another reason for incomplete powder rings are parasitic diffraction phenomena (see Section 3.3). Areas on the detector affected by these phenomena have to be excluded from the integration. The integration of incomplete rings is performed in the same way as it is done for complete rings, except that excluded areas are skipped. After the integration, a different scale factor has to be used, which takes into account that the effective length of the integration curve is shorter than for complete rings. At least one half of a powder ring should be available for integration, in order to obtain its intensity with sufficient accuracy. All necessary scalings are automatically made in the integration process of FIT2D, and the resulting data of intensity *versus* diffraction angle  $2\Theta$  or  $d$ -spacing is equivalent to data obtained with a point detector. Additional information on how the integration of an image plate recording with FIT2D is performed, is given in Section 3.5.

## 3.2 Startup

In this and the subsequent sections data of  $\text{Nb}_3\text{Te}_4$  (Chapter 5, Fig. 3.3) are used to illustrate problems that are commonly encountered during the data reduction with FIT2D. After starting the program the user has to specify the amount of memory, which will be used by FIT2D to store the image plate recording. The  $x$ -dimension of the memory array also defines the maximum number of points of the resulting one-dimensional data of intensity *versus* diffraction angle. The allocated memory should correspond to the size of the image in pixels (Table 3.1). A larger amount of memory can be allocated, but in FIT2D's standard graphical representation, the excess memory appears as a band of zero intensity around the images. This leads to erroneous intensity values, because the integration is extended into this zero-intensity area. Reproducible results can only be obtained when the dimensions of the allocated memory match the size of the image and

Figure 3.1: X-ray powder diffraction data of  $\text{In}_x\text{Nb}_3\text{Te}_4$  at ambient conditions, as it was recorded on a MAR3450 imaging plate detector. The sample was contained in a glass capillary of diameter 0.5 mm (irradiated volume  $0.02 \text{ mm}^3$ , beam size  $0.2 * 0.2 \text{ mm}^2$ ). The wavelength of the radiation was  $0.13918 \text{ \AA}$ . The small white area in the center of the image is a shadow cast by the beam stop assembly.



Figure 3.2: X-ray powder diffraction data of  $\text{In}_x\text{Nb}_3\text{Te}_4$  at 0.26 GPa, recorded on a MAR3450 imaging plate detector. The sample was contained in a diamond anvil cell (irradiated volume  $0.001 \text{ mm}^3$ ). The wavelength of the radiation was  $0.43133 \text{ \AA}$ . The white area in the center of the image is a shadow cast by the beam stop assembly.



Figure 3.3: X-ray powder diffraction data of  $\text{Nb}_3\text{Te}_4$  at 0.495 GPa, recorded with an online image plate detector (Thoms et al., 1998). The sample was contained in a diamond anvil cell. The wavelength of the radiation was  $0.37380 \text{ \AA}$ . The vertical streak, about 2 cm right of the left edge of the image may be due to a change of the sensitivity of the detector. The light gray area in the top left quadrant of the image is a shadow cast by the beam stop assembly.



Table 3.1: Comparison of the image plate formats used in this work. Mar3450 and Mar2300 are generated by the Marresearch Mar345 detector. ".DAT" is a free binary format that is generated by the online image plate detector, which was available at beamline ID30 (Thoms et al., 1998). n/a means that the information is not required in FIT2D, since the format is automatically recognized.

	Mar3450	Mar2300	".DAT"
automatically recognized	yes	yes	no
image size - x [pixels]	3450	2300	3024
image size - y [pixels]	3450	2300	3728
pixel size - x [ $\mu\text{m}$ ]	100	150	77.06
pixel size - y [ $\mu\text{m}$ ]	100	150	80.11
record type	n/a	n/a	integer 2 byte
integer type	n/a	n/a	signed
swap bytes	n/a	n/a	yes
Start data at byte	n/a	n/a	1

the full image is displayed (FULL UNZOOM). However, an increase of the  $x$ -dimension can be useful, since it allows better oversampling (see Section 3.5).

Image plate recordings in several different formats can be read by FIT2D. Some formats are automatically recognized (Table 3.1). For other formats the exact values of the image dimensions, along with information about the data records have to be supplied manually. If the image is not displayed correctly, the reason is most probably a wrong value for one of these parameters. During input of the data, one can also select, whether a flat field correction and a spatial distortion correction will be applied to the image. The flat field correction has to be applied, if different areas of the image plate detector have a different sensitivity. The correction is calculated using an image of the detection area uniformly exposed with radiation of the same wavelength, which has been used in the acquisition of the image for that the correction is intended. The correction image should be available at the beamline. However, because of the difficulties generating a large uniformly irradiated area, it seems to be troublesome to obtain a reliable correction image and often the beamline scientists cannot provide such an image. Moreover, it would only be valid for a short duration, since the sensitivity of image plate may change with age.

To correct for spatial distortion, a well defined grid mask is placed directly in front of the detector and an image of this mask is recorded. The correction is made by comparing the recorded image to the mask itself. More details on the correction procedures can be found, *e.g.*, in Stanton et al. (1992). Modern detectors, like the MAR3450, have been calibrated during assembly and the man-

ufacturers claim that these calibrations are valid for the lifetime of the detector. Therefore, no additional calibration is necessary for these detectors.

The image plate recordings used in this thesis were obtained using a MAR3450 detector and an online image plate reader designed at beamline ID30 of the ESRF (Thoms et al., 1998) (denoted as Thoms detector). No flat field and spatial distortion corrections were applied to the data collected with the MAR3450 detector. Data collected with the Thoms detector, were only corrected for spatial distortion. A flat field correction would also be required (Fig. 3.3), but it had to be omitted, because no flat field correction file was available.

### 3.3 Using Masks

As already indicated in Section 3.1, it is sometimes necessary to exclude areas of the image plate recording from the subsequent steps of the data reduction. These phenomena will be discussed in the next paragraphs. Several tools, denoted as masks, exist in FIT2D, which are used to define an overlay for an image. Pixels located below the overlay are subsequently excluded from any data processing procedures, but the image itself is not changed. There are circular masks (denoted peak masks) in several different sizes. These masks are most convenient to exclude small, isolated areas of the image. Larger, continuous areas can be excluded by drawing a free-form polygonal region using the polygon mask tool. These two types of masks have to be applied manually, but there is also an automatic mask, the so called threshold mask. When this mask is used, the image is searched for pixels, whose intensities are above or below (can be specified) a given threshold value and all pixels that fulfill the criterion are masked. Finally, two tools (unmask peak and unmask polygon) are available to delete or modify already defined masks.

#### 3.3.1 Objects in the beam path

When scattered or diffracted radiation hits a solid object, the radiation is blocked and a shadow of the object is cast on the detection area. Sources of these shadows can be the beam stop assembly (Figs. 3.1, 3.2 & 3.3) or the diamond anvil cell, if it is not properly aligned. Since these objects are usually made of metal, all radiation, including sections of the Debye-Scherrer cones, that interacts with the objects is absorbed, but depending on the distance of the object from the detector, some amount of scatter radiation reaches the detector in the shaded areas. The intensities in the shaded areas are completely unrelated to the intensities in the non-shaded parts of the image. *E.g.* in the experimental setup, which was used to record the image shown in Fig. 3.2, the beam stop assembly was directly in front of the imaging plate and in the shaded area an intensity of  $33 \pm 3$  counts is

measured, while the background intensity in a non-shaded area is about  $680 \pm 10$  counts. In the experiment, where the image of Fig. 3.3 was recorded, the beam stop was several cm away from the detector and intensities of  $550 \pm 50$  counts are measured in the shaded area *versus*  $1700 \pm 100$  counts in the background outside the shadow.

All types of shadows result in a different (lower) background. Circular shaped shadows, which are centered at the beam center can be problematic, if Debye-Scherrer rings lay under a shaded area. If not treated, the corresponding Bragg reflections would have an intensity of zero. (Of course, due to the behavior of the background one knows that the "zero" is an artifact). Irregularly shaped shadows which cut off only parts of the powder rings, also introduce systematic errors into the peak intensities, but the background does not show a characteristic behavior. Thus one can not identify that these peak intensities are wrong (Fig. 3.4). In FIT2D, the polygon mask tool is most convenient to mask the beam stop assembly (Fig. 3.5). In this particular case the mask has also a positive effect on the profile fitting, since after masking the beam stop, the background around the first Bragg peak becomes straight and is thus more easy to define (Fig. 3.4).

### 3.3.2 Overexposed spots

The components of an image plate detector system, especially the photomultiplier, impose a limitation to the dynamic range of the detector. The detection process in an image plate detector works as follows: X-rays interact with  $\text{Eu}^{2+}$  ions, which are present in a layer of (usually)  $\text{BaFBr:Eu}$  in the image plate. The  $\text{Eu}^{2+}$  are ionized to  $\text{Eu}^{3+}$  and fast electrons are generated. These electrons become trapped close to their point of origin at sites with anion vacancies. The amount of trapped electrons is proportional to the intensity of the X-rays. During read-out, the image plate is scanned pixel by pixel with red light from a He-Ne laser. The red light causes the electrons to leave the traps and to recombine with the  $\text{Eu}^{3+}$ , thereby emitting blue luminescence radiation. The intensity of the luminescence radiation is proportional to the amount of previously trapped electrons, *i.e.* it is proportional to the intensity of the X-rays. For each pixel the intensity of the luminescence light is measured with a photomultiplier; the output signal of the photomultiplier is digitized and stored. The MAR3450 detector uses data records with a length of 17 bits (0 to 131071) to store the intensity information of one pixel, while the Thoms detector uses data records of 14 bits (0 to 16383). The level of intrinsic noise of an image plate detector system is very low and weak signals (single photons) can be detected. The detector shows a linear response to the detected signal over its complete dynamic range, which encompasses five or six orders of magnitude. (The non-linearities of the photomultiplier are compensated during digital data processing.) Above a specific intensity level however, the response of the photomultiplier becomes independent of the initial intensity

Figure 3.4: The scattered intensity of  $\text{Nb}_3\text{Te}_4$  as a function of the scattering angle  $2\Theta$ , obtained from the integration of image plate recordings. The dashed line corresponds to an image, which was integrated without applying any corrections (Fig. 3.3), while the solid line corresponds to data where the area shaded by the beam stop was excluded (Fig. 3.5). Note the different background- and peak intensities at lower angles.

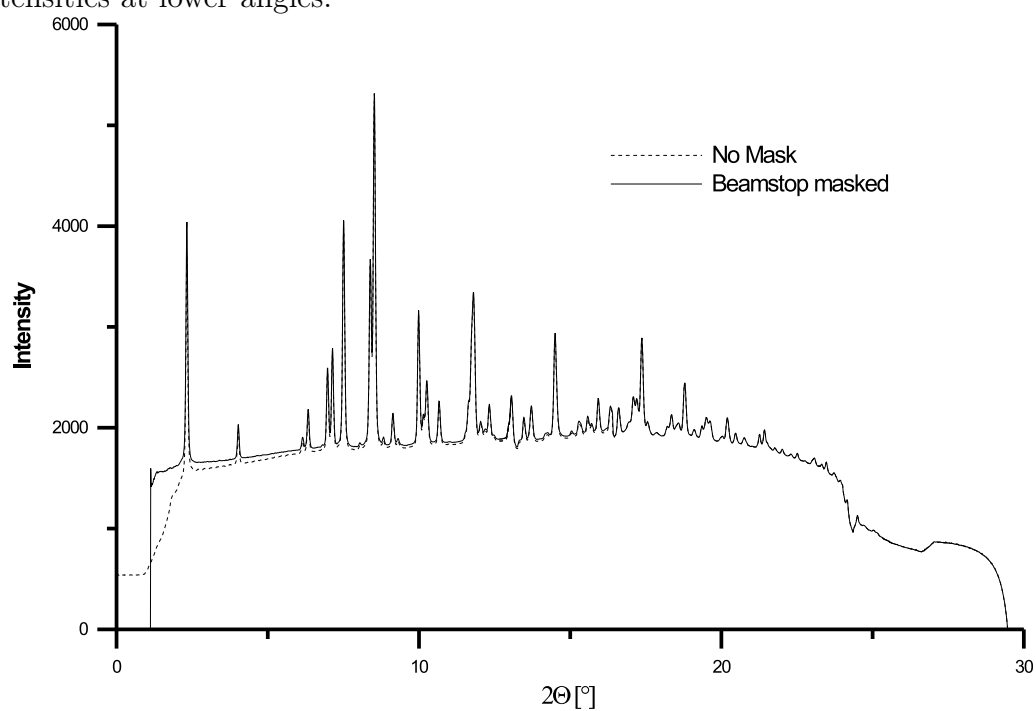


Figure 3.5: Application of a polygon mask to the image of Fig. 3.3, with the purpose to exclude the regions affected by the shadow of the beam stop from the integration. The masked area is colored in white.



and a constant output is obtained. Here the photomultiplier is saturated. The same intensity is found for all pixels, where a saturation of the photomultiplier has occurred. This intensity corresponds to the maximum value expressible in a data record. Affected pixels are denoted as overexposed pixels; an area consisting of overexposed pixels is denoted as overexposed spot or overexposed area. It is noted that in overexposed areas blooming can occur.<sup>1</sup> Therefore, pixels adjacent to overexposed areas also appear more intense than they would be based on the detected amount of radiation.

On image plate recordings collected in X-ray powder diffraction at high pressures, overexposed areas can be found in single crystal diffraction spots, which originate at the diamond anvils (see next section). They can also be found as the maxima of diffraction spots of very large crystallites of the powder sample and in this case they are located on the Debye-Scherrer rings or very closely nearby<sup>2</sup> (Fig. 3.6). It must be noted, that overexposed spots can be much more intense than average spots on the powder rings. It is possible that the intensity at the non-overexposed flanks of overexposed spots is higher than at the center of average spots. So, even if there are only a few overexposed spots on each powder ring, they can have a huge impact on the peak intensities of the integrated data of intensity *versus* diffraction angle and they are a source of systematic errors. Overexposed spots are also a source of peak broadening or the reason of irregular peak shapes. It is thus necessary to exclude not only overexposed pixels, but also the region round the overexposed pixels. *I.e.*, in the case of a well defined diffraction spot with an overexposed center, the complete spot must be excluded. While significant differences of the peak intensities are observed prior to and after the exclusion of overexposed spots (Fig. 3.7), the removal of additional segments of the Debye-Scherrer rings (about 30°) does not change peak intensities visibly.

Finding overexposed areas with FIT2D is straightforward, if a threshold mask is used (Fig. 3.6). The value of the threshold depends on dynamic range of the detector. For the Thoms detector a value of 15000 and for the MAR3450 detector a value of 100000 have been used.<sup>3</sup> After the overexposed areas have been found, the environment of the overexposed spots can be masked using a peak mask or a polygon mask (Fig. 3.8).

---

<sup>1</sup>Blooming denotes the migration of the electrons to adjacent pixels, where they cause secondary ionization of Eu. In an imaging plate this may occur when a large amount of electrons is generated simultaneously, *e.g.* when the signal is strong enough to cause saturation of the detector.

<sup>2</sup>The lattice strain can be different for large crystallites than it is for crystallites of average size. Therefore there can be slightly different lattice parameters.

<sup>3</sup>These values were smaller than maximum possible values to account for noise and the fading of the image.

Figure 3.6: Excerpt of the image of Fig. 3.3 with the overexposed spots marked as white areas. The overexposed spots are part of the powder rings. They were found by the application of a threshold mask.

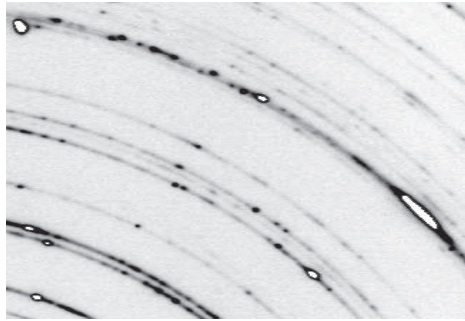


Figure 3.7: The scattered intensity of  $\text{Nb}_3\text{Te}_4$  as a function of the scattering angle  $2\Theta$ , obtained from the integration of image plate recordings. The dashed line corresponds to an image, where the area shaded by the beam stop was excluded (Fig. 3.5), while the solid line corresponds to data where additionally overexposed spots were excluded (Fig. 3.8). Note the different intensities of the Bragg peaks.

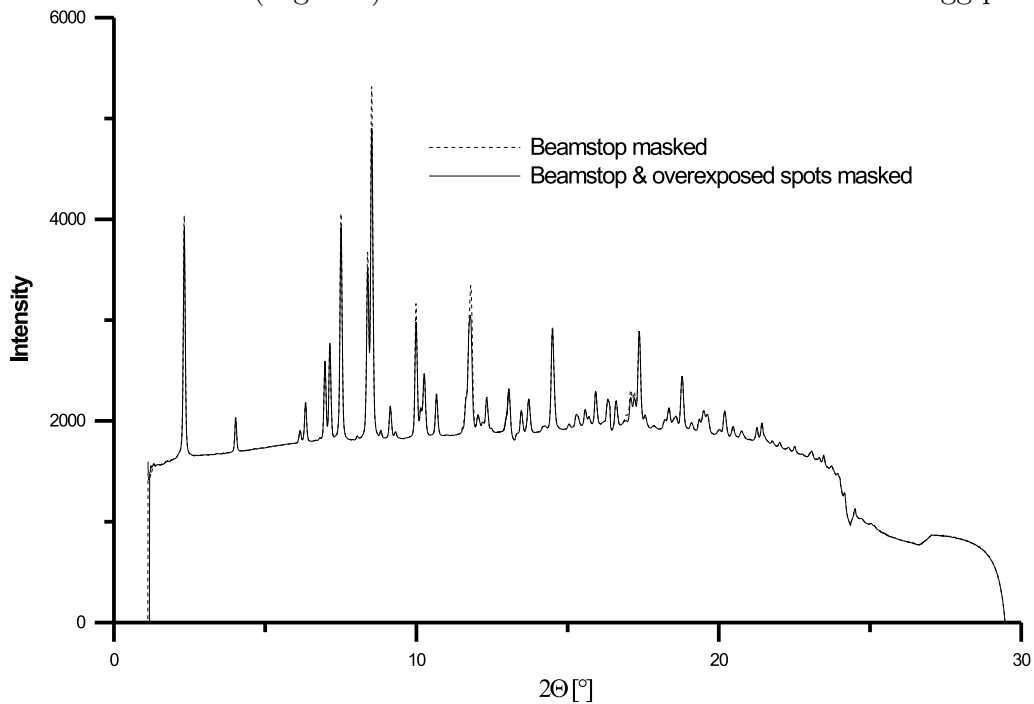


Figure 3.8: Image of Fig. 3.3 after subsequently applying several masks. Firstly, a polygon mask was used, with the purpose to exclude the regions affected by the shadow of the beam stop from the integration. Next a threshold mask was applied, to exclude overexposed areas and finally a peak mask was applied multiple times to exclude the areas around overexposed spots on the powder rings. The masked area is colored in white.

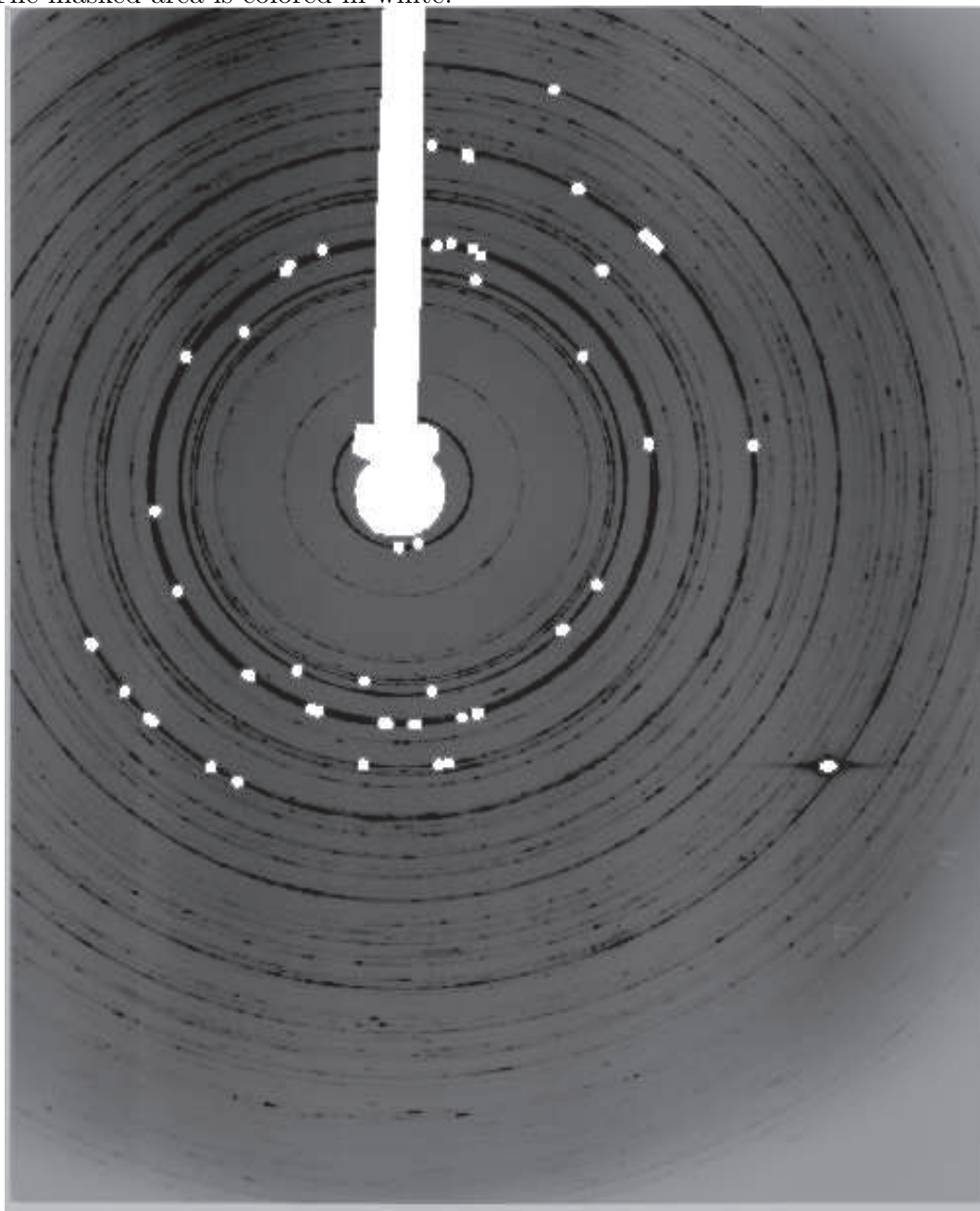
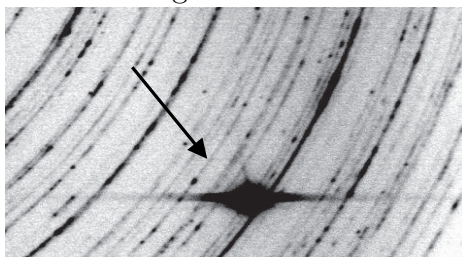


Figure 3.9: Excerpt of the image of Fig. 3.3 showing a diamond single crystal reflection. Note the streaks that originate at the diffraction spot.



### 3.3.3 Diffraction from impurity phases

In high-pressure diffraction experiments, different materials are exposed to the radiation and contributions of all of these phases can be found in the diffraction data. Air scattering and scattering by the (amorphous) pressure transmitting medium contribute to the background. This is usually not treated at this stage of the data reduction (see Section 3.6).

There are contributions of at least two additional crystalline phases - the diamond anvils and the pressure calibration standard - present at all times. The diamond anvils consist of large single-crystalline diamonds and in the diffraction image, their contributions appear either as very intense and broad spots (Fig. 3.9) or as diffuse streaks and Kossel lines. Diamond spots can appear anywhere on an image, but due to their high intensities and their size, they can be identified easily, even if they overlap with the powder rings.

For the pressure calibration using the ruby luminescence method, a small single crystal of ruby is inserted into the sample volume. The size of the ruby is not much larger than the average grain size of the polycrystalline sample and on an image plate recording, the ruby spots have about the same intensities as diffraction spots of typical powder grains of the sample. Like diamond reflections, the ruby spots appear at random locations on the image, but an identification is only possible, if they are isolated and not overlapping with a powder ring (Figs. 3.10 & 3.11) (Overlap has to be resolved at a latter stage of the data processing, see Section 3.6). However, in the integrated powder pattern of intensity *versus* diffraction angle, one cannot distinguish, if a particular Bragg peak corresponds to a real powder ring, or if it corresponds to an isolated diffraction spot of a single crystalline impurity phase (Fig. 3.12) and thus these diffraction spots should be excluded from the image prior to the integration.

For pressure calibration using an internal standard, the standard material, which is polycrystalline, is mixed into the sample and all that is stated here also applies to other polycrystalline impurity phases, which can be *e.g.* a crystalline pressure medium or impurities of the sample. In the diffraction pattern, a poly-

Figure 3.10: Excerpt of the image of Fig. 3.3 showing an isolated diffraction spot originating from a single crystalline impurity phase, most probably from one of the rubies.

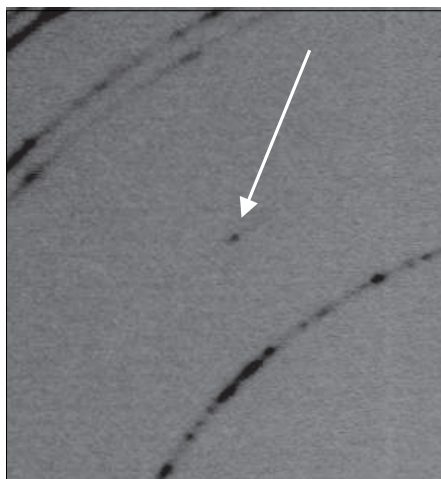


Figure 3.11: Excerpt of the image of Fig. 3.3 showing a single crystalline diffraction spot close to a powder ring. The origin of this spot is most probably a ruby.

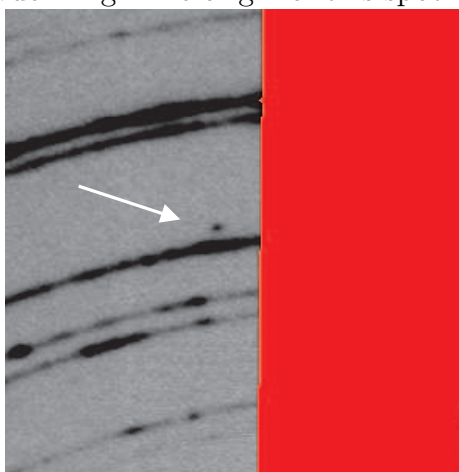


Figure 3.12: The scattered intensity of  $\text{Nb}_3\text{Te}_4$  as a function of the scattering angle  $2\theta$ , obtained from the integration of image plate recordings. The dashed line corresponds to an image, where the area shaded by the beam stop and overexposed spots were excluded (Fig. 3.8), while the solid line corresponds to an image where also the diffraction spots originating from impurity phases and minor errors as described in Section 3.3.4 were excluded (Fig. 3.14). Note the absence of the peak at about  $9^\circ$  and at about  $17^\circ$  in the latter data.

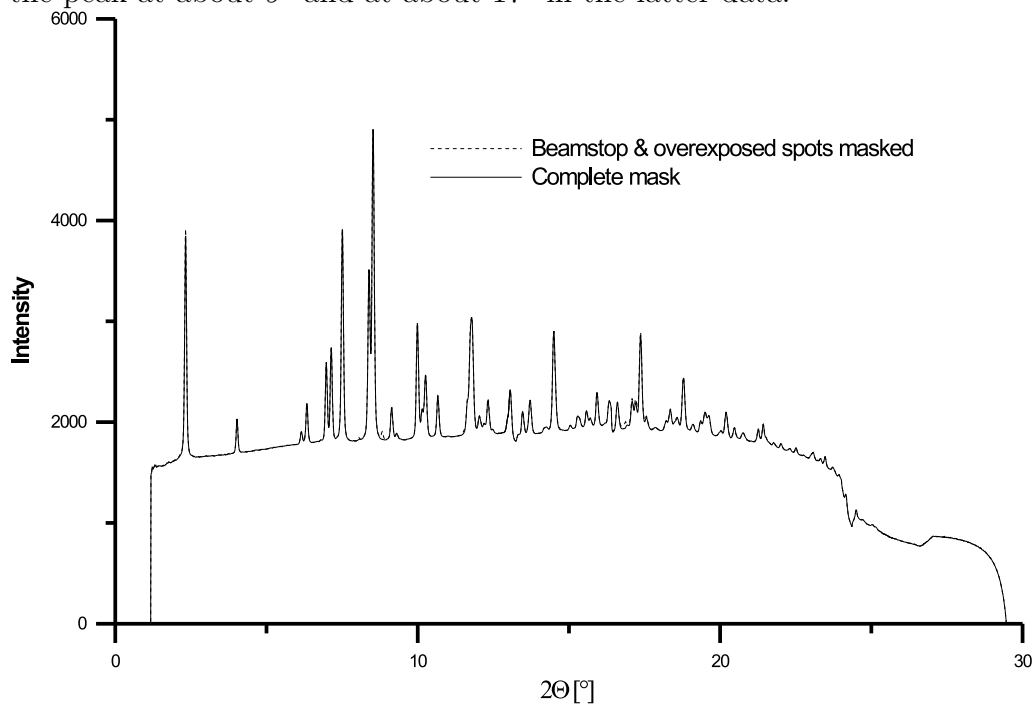
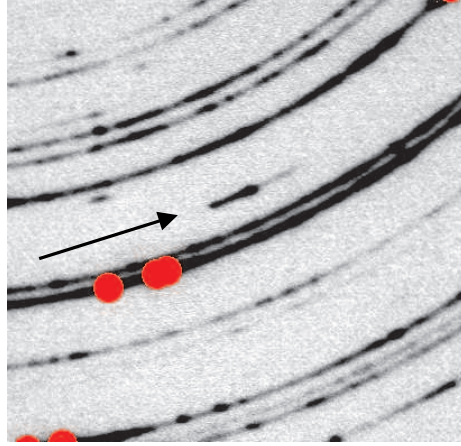


Figure 3.13: Excerpt of the image of Fig. 3.3 showing diffraction of a polycrystalline impurity phase with strong texture.



crystalline impurity phase appears as an additional set of Debye-Scherrer rings. A distinction between the different phases in the image plate recording is possible only under a few favorable conditions. It is most easy, if the number of particles of the sample is much larger than the number of crystallites of the standard or when the impurity phase shows a high degree of texture. In this cases, the additional rings are more discontinuous than the powder rings of the sample, or the rings only consist of a few spots (Fig. 3.13). If required, such "rings" can even be excluded from the integration. If the different phases have similar particle statistics but a different crystallinity, resulting in different widths of the powder rings for each phase, a distinction of the different phases can also be possible. In other cases, a distinction of different phases using only one image is not possible. An identification of all phases can be made if two or more images are used, recorded at different pressures or temperatures, if structural phase transitions occur or if the materials have different compressibilities. However, only powder rings, which do not overlap, can be identified by using one of these methods. In the case of overlap, or if the impurity phase is required (pressure calibration), other ways to handle impurity phases have to be used (see Section 3.6).

Isolated single crystal spots or strongly textured Debye-Scherrer rings of impurity phases can be excluded with FIT2D using either peak masks or polygon masks, depending on the size of the diffraction spots (Fig. 3.14).

### 3.3.4 Miscellaneous minor defects

In addition to the phenomena discussed in the Sections 3.3.1 – 3.3.3, other areas with incorrect intensities can be found on an image plate recording. Often, these defects are due to the instrument or the diffraction setting. If radiation, which

Figure 3.14: Final mask (white areas) superimposed on the diffraction image of Fig. 3.3. It defines the areas to be excluded from the integration. The mask includes regions affected by the shadows of the beam stop, overexposed areas, diffraction spots of impurity phases and the diamond anvil cell, and miscellaneous minor defects (see Section 3.3.4).

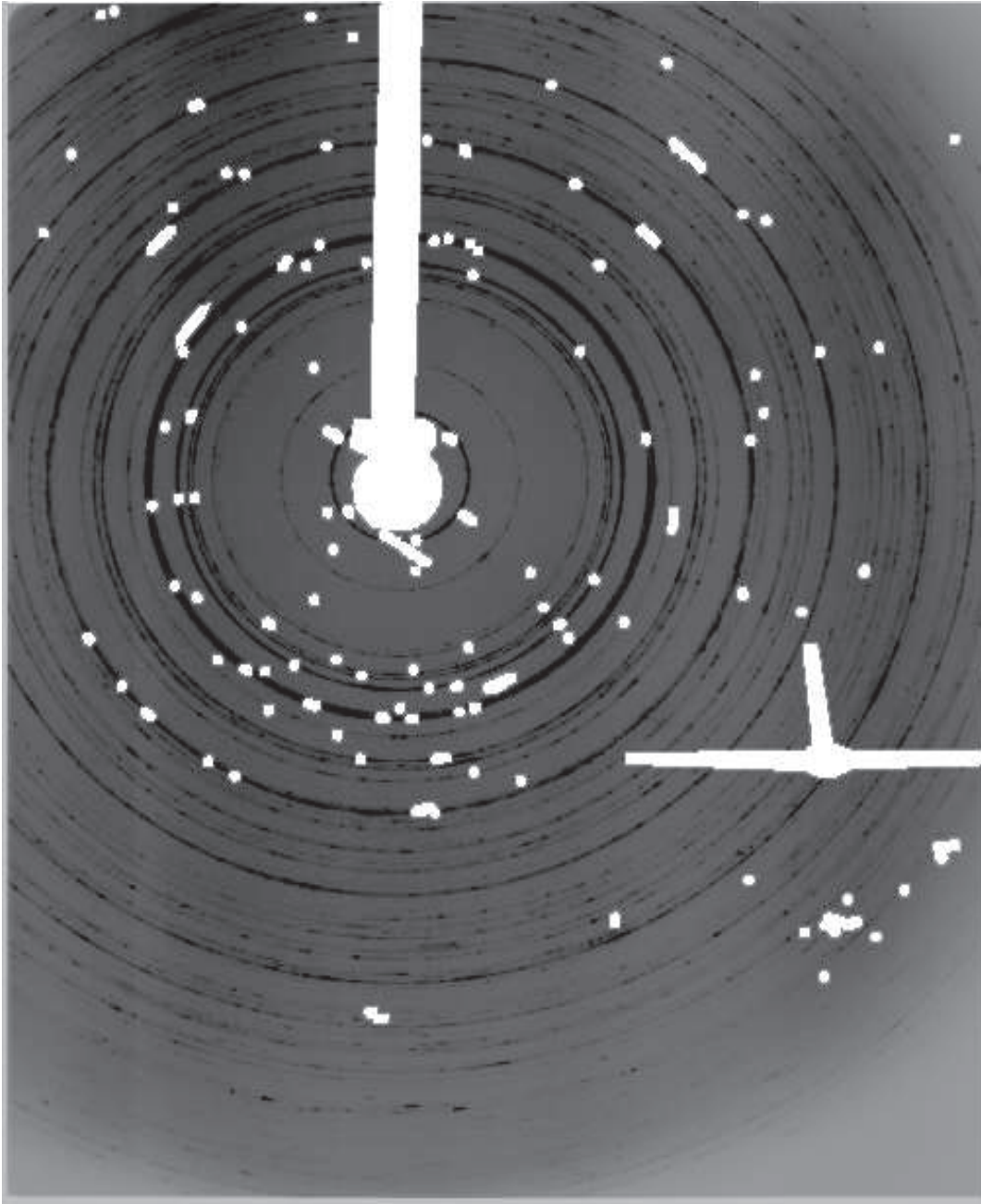
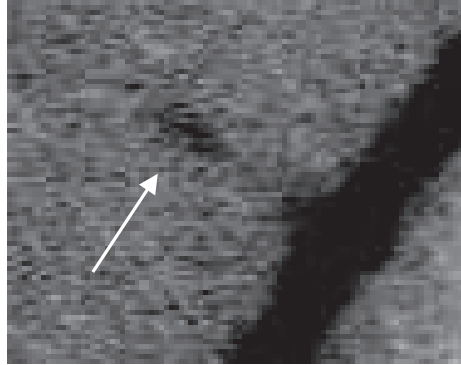


Figure 3.15: Excerpt of the image of Fig. 3.3 showing a diffuse peak or streak next to the innermost powder ring. It is probably due to radiation scattered at the beam stop.



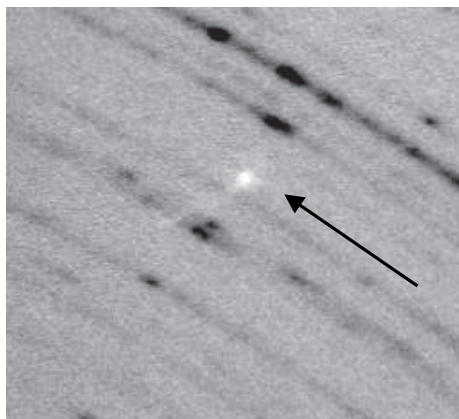
was scattered at the beam stop, hits the detection area, diffuse streaks pointing in the radial direction can be observed close to the beam center (Fig. 3.15). Dust on the backside of the diamond anvil or on the image plate, or a defect of the image plate, if a flat field correction was not performed, can appear as a point like shadow on the image (Fig. 3.16). Fortunately, these phenomena are not very frequent and thus they hardly influence the intensities of the integrated powder pattern (Fig. 3.12). Nevertheless they should be removed prior to the integration of the image plate data.

### 3.4 Calibration

As already discussed in Section 3.1, four parameters describing the geometry of the Debye-Scherrer rings on the detection plane (two coordinates of the beam center, tilt angle and tilt plane rotation angle) and two parameters describing the instrumental setup (wavelength of the radiation and sample to detector distance) must have been determined before the integration of a image plate recording of powder diffraction data can be performed and data of intensity *versus* diffraction angle  $2\Theta$  or  $d$ -spacing can be obtained. There are two different ways in FIT2D to determine these parameters.

For a series of measurements, which were all made using the same setup, it is sufficient, to do the calibration only once and then use the values obtained in the calibration for all other measurements. This applies to all the high-pressure series reported in this thesis, since during a series, the position of the sample the wavelength or the alignment of the detector were not changed. For the two high-pressure series of  $\text{Nb}_3\text{Te}_4$  however, the position of the beam center and the tilt angles were determined individually for each image, because there was no

Figure 3.16: Excerpt of the image of Fig. 3.3 showing a point shadow appearing at a random location of the image. Its origin is either a defect on the imaging plate or dust on the backside of the diamond anvil.



experience with the detector and the stability of the alignment. For the images of a single series, the refined positions of the beam center were in good agreement, and also the values of the tilt angle were all close to zero. Larger deviations between the individual values of the tilt plane rotation angles were found but these deviations are regarded to be artificial because in the limit of zero tilt angle, the tilt plane rotation angle is meaningless and the observed change of the "ellipticity" of the powder rings are more likely due to sample related effects that change the distribution of intensity on the powder rings rather than a shift of the detector.

### 3.4.1 Calibration using an external standard

All six geometrical parameters can be determined in a single step using an external standard, *i.e.* using a material whose lattice parameters and symmetry are known. To be able to use the procedure described here, an additional powder diffraction experiment has to be performed (calibration measurement) in which a sample is the standard material. The instrumental conditions must be the same for the calibration measurement and the actual experiment. So each time the sample-to-detector distance or the wavelength of the radiation is changed, a new calibration measurement is required. FIT2D only allows standard materials, for which information about the indexing was coded into the program. The list currently includes  $\text{Al}_2\text{O}_3$ ,  $\text{LaB}_6$ ,  $\text{NaCl}$ ,  $\text{CeO}_2$ , Silicon and Paraffin wax. After the image plate recording is read into the program and the corrections for parasitic diffraction phenomena (Section 3.3) has been performed, the "calibrant" subroutine is invoked and the standard is specified. The user has to provide

starting values for the wavelength of the radiation and the sample to detector distance and one can select the parameters to be determined in the calibration procedure. However, the wavelength and the sample-to-detector distance are highly correlated and they cannot be determined together if a cubic standard material, *e.g.* silicon or  $\text{LaB}_6$ , is used. Therefore one of them, usually the wavelength, is measured by different methods and it is kept fixed. At the high-pressure beamlines of the ESRF, the wavelength calibration is made by the beamline scientist. This measurement involves a time-consuming procedure and usually a single wavelength is used for all experiments. The sample-to-detector-distance can be obtained by measuring it manually and the value obtained in this way is sufficiently accurate to be used as a starting value for calibration routine.

In the next step of the calibration procedure, the position of the innermost powder ring of the standard has to be marked on the diffraction image. This is done by selecting several points of the ring in the graphical representation of the image on the computer monitor. FIT2D only needs a few points, but to increase the accuracy, more than the requested points should be given. About ten points are sufficient. The points should be distributed homogeneously over the powder ring. The procedure continues automatically and the program calculates and suggests two sets of parameters, which are written to the terminal (in the UNIX version). The user has to select one, usually the one which has smaller standard uncertainties.

One must be aware, that the calibration is perfectly correct only for the standard measurement. When the sample is replaced, the sample-to-detector distance can change by an unspecified, however very small amount and by using the value obtained during the calibration, small systematic shifts of the diffraction angles and the the lattice parameters can be introduced. This does not apply to the relative shifts of lattice parameters, which were obtained from a series of measurements taken at different temperatures or pressures, as long as the sample has not been moved.

### 3.4.2 Standard-free calibration

If a calibration measurement does not exist, like it was the case for the two high pressure series on pristine  $\text{Nb}_3\text{Te}_4$  described in this thesis (Chapter 5), the four parameters describing the geometry of the Debye-Scherrer rings can be determined in FIT2D for any diffraction image from the image itself. However, the wavelength of the radiation and the sample-to-detector-distance have to be known beforehand. The alternative calibration procedure is invoked by the "tilt" command and the information required on the first two screens of these routine has to be provided by the user. Several methods to find the beam center are available here, with the "circle coordinates" or the "ellipse coordinates" procedure being most appropriate. Both routines work in the same way. In a first step, one has to identify

a powder ring in the image. The procedure is almost analogous to specifying the innermost powder ring in the calibration using a standard. Here however, it is possible to select any powder ring, so a non-overlapping strong ring should be selected, which is completely on the image. After an appropriate number of points on the ring and a cutoff range, which specifies two limit radii between those the ring is found, additional powder rings can be indicated to be included in the calculation to obtain higher accuracy. The procedure concludes automatically and presents two solutions, from those the better one, having smaller errors, should be chosen.

### 3.5 Integration

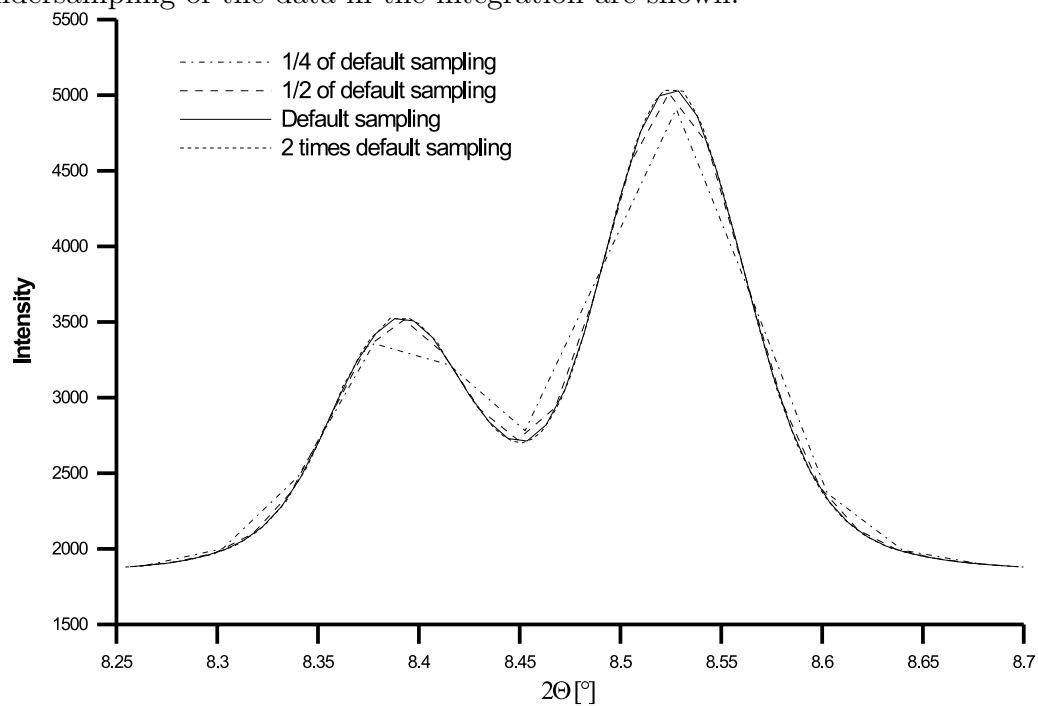
The integration of image plate recordings of powder diffraction data is made almost automatically in FIT2D after the excluded areas have been defined and the calibration is completed. By invoking the "integrate" command, the routine is started. After the required parameters (see Sections 3.1 and 3.4) have been given, the desired format of the integrated data has to be specified. For data of intensity *versus* the diffraction angle  $2\Theta$  the "intensity conservation" option has to be disabled and the "geometrical correction of intensities" option has to be enabled. Finally the number of points of the integrated data ("number of bins in output scan") has to be given. FIT2D proposes a default value, which usually is about the horizontal size of the image in pixels. When this value is used, like it was done for all data used in this thesis, the maximum amount of information, which can be extracted from image plate data, is present in the integrated data. Using a larger value (oversampling) does not significantly improve the quality of the integrated pattern (Fig. 3.17), it merely increases the size of the data file. Using a smaller value (undersampling) may lead to loss of information and it may provide false intensities (Fig. 3.17).

### 3.6 Using Integrated Image Plate Data in Structure Refinements

Powder diffraction data that has been obtained by integrating image plate recordings with FIT2D can be used for structure refinements just like conventional powder diffraction data obtained by a point detector, if a few things are kept in mind.

- Format of the data: The integrated powder diffraction data should be saved in a format that stores the profile using one number that represents the diffraction angles or the  $d$ -spacing and another number that represents the intensity. The CHI-plot format is such a format. It can be read by

Figure 3.17: Detailed view of two peaks in a powder diffraction pattern which was obtained by integrating image plate data. The effects of oversampling and undersampling of the data in the integration are shown.



JANA2000 (Chapter 4), after the first few lines up to the line with the first data record have been deleted from the file. Other data formats, like the formats native to the Rietveld refinement programs GSAS (Larson & von Dreele, 1994) or Fullprof (Rodriguez-Carvajal, 2001) store only the intensity values and the diffraction angle or the  $d$ -spacing for each point is calculated from the value corresponding to the the first data record (starting value), the step size and the ordinal number of the record. If such a format is required, one has to make sure that during the conversion of the file formats the step size is calculated with sufficient accuracy. Otherwise, rounding errors can lead to angle-dependent zero shifts, or to discontinuities in the dependencies of the lattice parameters on pressure or temperature.

- Cutting off the edges of the data: As stated in Section 3.3 the intensities on an image plate recording found at regions shaded by the beam stop assembly are completely unrelated to the intensities found in non-shaded regions. This also applies to the integrated powder diffraction pattern (Figs. 3.4, 3.7 & 3.12). At high diffraction angles zero intensities are observed in these figures. This is due to the integration, which also included areas of the image outside the detection area of the image plate detector. At the beginning and at the end of the data file, all data which corresponds to these regions should be deleted. For any Bragg peaks in these areas, false intensities would be obtained. Also, the refinement of the background may fail, since most Rietveld refinement computer programs define the parameters of a background function at the lowest diffraction angles present in the data (*e.g.* in a shaded region) and apply them to the whole powder pattern. However, if data is removed from a powder pattern, great care has to be taken that no information are lost. *E.g.* in Fig. 3.12 at low angles, only the points with zero intensity and the points in the region, where the intensity increases rapidly, should be removed. At high angles only the points beyond the edge at  $29^\circ$  should be removed, while the region between the edges at  $24^\circ$  and at  $29^\circ$  should be kept and an attempt should be made to define a manual background for this region.
- Background: In high pressure experiments using diamond anvil cells, the background is usually very high and it varies with the diffraction angle. Functions with a few parameters cannot describe this background, and a combination of a manual background and a background function has to be used in the refinement.
- Impurity phases / peak overlap: The best way to treat multiple phases in a powder pattern is to perform simultaneously Le Bail fits or Rietveld refinements of all phases. In this way the most accurate peak intensities can be extracted from the powder pattern for isolated peaks and for overlapping

peaks. A drawback of this method is that it requires complete structural information about all impurity phases present in the powder pattern.

Rietveld refinement programs also allow to exclude areas of the powder pattern from the structure refinement. This can be used to exclude isolated peaks of impurity phases, whose crystal structures are not known. But peak overlap cannot be resolved with this method and false intensities can be assigned to the overlapping peaks.

- Peak asymmetry: Axial divergence (Finger et al., 1994) is one of the main sources of peak asymmetry in powder diffraction data, which were recorded using point detectors. Is not present for data obtained by integration of image plate recordings, because of the geometry of the detector setup and the method of the integration of the data (Section 3.1). Other sources of peak asymmetry remain, but their contributions can be considered as minor. Most of the time an empirical asymmetry correction is sufficient to describe the barely detectable peak asymmetry of the Bragg peaks.
- Correlations between parameters in the Le Bail fit and in the Rietveld refinement: In Le Bail fits and Rietveld refinements usually strong correlations between the lattice parameters, the zero shift, and the asymmetry parameter(s) are observed. These correlations make it difficult to analyze the relative shifts of lattice parameters, induced by a change of the pressure or the temperature, between different data collections. For the high-pressure and low temperature series reported in this thesis, this problem was solved by determining the values of the instrumental parameters (asymmetry, zero shift) for a single selected pressure or temperature and by applying these values to all other measurements of the same series.